Research Signpost
37/661 (2), Fort P.O., Trivandrum-695 023, Kerala, India

Physics of Solid State Ionics, 2006: 247-269 ISBN: 81-308-0070-5
Editors: Takashi Sakuma and Haruyuki Takahashi

8 Physical properties of perovskite-type lithium ionic conductor

Naoki Inoue and Yanhui Zou
Department of Physics, Faculty of Science, Ehime University, Matsuyama
Ehime 790-8577, Japan

Abstract

The purpose of this chapter is to understand the ionic conduction of perovskite-type oxides. It is based on the fundamental theories of perovskite structure, ionic conductivity, conductivity measurement, X-ray diffraction and Rietveld analysis, and nuclear magnetic resonance (NMR). Typical examples of lithium ionic conductor are introduced.

Introduction

Perovskite-type oxides have been considered to be important materials due to their potential applications, such as lithium ion batteries, solid oxide fuel cells, and oxygen sensors, etc [1-6]. To understand the

Correspondence/Reprint request: Dr. Naoki Inoue, Department of Physics, Faculty of Science, Ehime University, Matsuyama, Ehime 790-8577, Japan. E-mail: naokinoue@phys.sci.ehime.ac.jp

physical properties of ionic conductor, the crystal structure of perovskite-type oxides, basic theories of ionic conduction, conductivity measurement [6-7], X-ray diffraction [8], Rietveld analysis [9,10] and NMR [11-17] are discussed.

Section 2 deals with the crystal structure of perovskite-type oxides. Section 3 deals with the subjects of ionic conduction and conductivity measurement, and an example of lithium ionic conductor. Section 4 deals with the principles of X-ray diffraction and Rietveld analysis. Section 5 deals with the basic theory of NMR. Basically, there are some quantities including high resolution NMR spectrum, those are the chemical shifts dependent on the chemical environment, the line-widths dependent on the ionic motion, spin-lattice and spin–spin relaxation times, quadrupole interaction etc. Quadrupole effect reflects the information about local symmetry. Section 6 deals with the summary.

1. Perovskite-type oxides structure

Figure 1 shows the structure of perovskite-type oxide with the general formula ABO_3. These oxides can tolerate different ions in A- and B-sites. The coordination numbers of A- and B-sites are 12 and 6, respectively. In the idealized perovskite-type oxide, the structurally related parameters have the relation

$$r_A + r_O = \sqrt{2}(r_B + r_O) \tag{1}$$

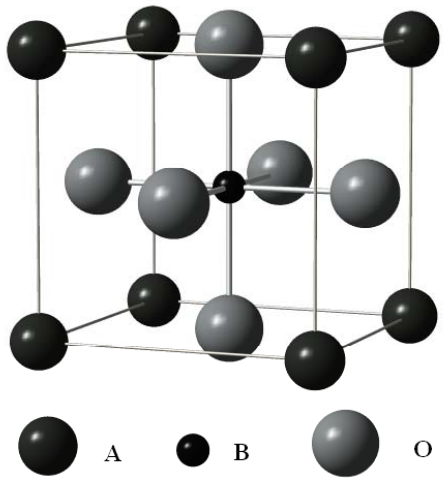

Figure 1. Perovskite-type oxides structure.

where r_A and r_B are the ionic radii for cations of A- and B-sites, respectively, and r_O is the radius of oxygen ion. But, in order to characterize the real perovskite-type oxide, we use the parameter of tolerance factor as

$$t = (r_A + r_O)/\sqrt{2}(r_B + r_O). \quad (2)$$

In many compounds of perovskite-type oxide, the parameter of t is in the range of 0.8 to 1.0. When the host ions A and B are replaced by allo-valent ions, the charge neutral compensation is needed. The defect concentration in the perovskite-type oxide is either increased or decreased depending on different types of allo-ion and their concentrations.

Materials of perovskite-type structure have a large variety of properties: $CaZrO_3$, $SrTiO_3$ and $SrZrO_3$ are proton conducting materials, and the solid solutions $La_{4/3-y}Li_{3y}\square_{2/3-2y}Ti_2O_6$ (LLTO) are lithium conductors with vacant defects $\square_{2/3-2y}$ in which the conductivity is about 10^{-3} S/cm at room temperature [4]. In this compound, La^{3+} ions are located in A-site and Ti^{4+} ions in B-site.

2. Ionic conduction

2.1. Conductivity

The stationary electric current J induced by the electric field $\partial\phi/\partial x$ is

$$J = -\sigma\frac{\partial\phi}{\partial x} \quad (3)$$

$$\sigma = Zen\mu \quad (4)$$

where σ is the conductivity, Z the valence number, e the charge of electron, n the concentration of charged carriers per unit volume, and μ the mobility (the velocity per unit field). We consider an ionic crystal of the composition MX. Positive and negative ion vacancies may be produced by successive jumps of both ions. A positive and a negative ion vacancy will attract each other due to the Coulomb interaction. This is called by Schottky defect. According to Kröger's notation, the generating process can be expressed by

$$Null \leftrightarrows V_M^{'} + V_X^{\bullet} \quad (5)$$

where $V_M^{'}$ and $V_X^{\bullet}$ are each ion vacancies.

The vacancy numbers $[V_M^{'}]$ and $[V_X^{\bullet}]$ in the equilibrium are represented by

$$[V_M^{'}] = [V_X^{\bullet}] = \sqrt{C_S}\exp(-\frac{H_S}{2k_BT}) \quad (6)$$

$$C_S = N^2 \exp(\frac{S}{k_B}) \tag{7}$$

where N is the number of lattice site, H_S the enthalpy required to form Schottky defect, S the entropy change due to the formation of Schottky defect, k_B the Boltzmann constant and T the absolute temperature. The mobility is given by

$$\mu = (\frac{Ze\lambda^2 K_m}{6k_B T}) \exp(-\frac{H_m}{k_B T}) \tag{8}$$

$$K_m = f_0 \exp(\frac{S_m}{k_B}) \tag{9}$$

where λ is a jumping distance, H_m the energy to be activated by jumping process, f_0 the attempt frequency and S_m the entropy change for jumping process. Therefore, the conductivity is equal to

$$\sigma = \sqrt{C_S}(\frac{Ze\lambda^2 K_m}{6k_B T}) \exp(-\frac{H_m + 0.5H_S}{k_B T}). \tag{10}$$

It also could be expressed by the Arrhenius's formula

$$\sigma = \frac{\sigma_0}{T} \exp(-\frac{E_a}{k_B T}) \tag{11}$$

where σ_0 is the pre-factor and E_a the activation energy.

2.2. Conductivity measurements

The alternating current method is useful because the measurement of electric impedance will give a frequency-dependent complex resistance (Cole-Cole plots) for conducting materials. A typical equivalent circuit can be expressed by Fig. 2, where R_1 is the bulk resistance, C_1 the bulk capacitance, R_2 the grain boundary resistance, C_2 the grain boundary capacitance, and R_3 the electric double layer resistance, $Z_W\{=(1-i)A/\sqrt{\omega}\}$ the Warburg impedance and C_3 the capacitance at electrode/sample interface, respectively [6,7]. Figure 3 shows Cole-Cole plots for the model in Fig. 2. Here, Z' and Z" show real and imaginary parts of resistance, respectively. The Cole-Cole plots obtained consist of two semicircles in the region of high frequencies. In low frequency the resistance increases with decreasing frequency due to the effect of electrode/sample interface. The semicircles in Fig. 3 are caused by two

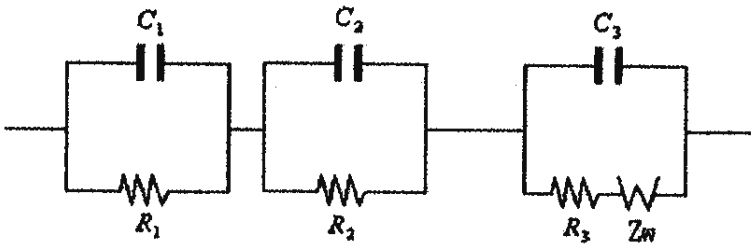

Figure 2. A typical equivalent circuit for ionic conductor.

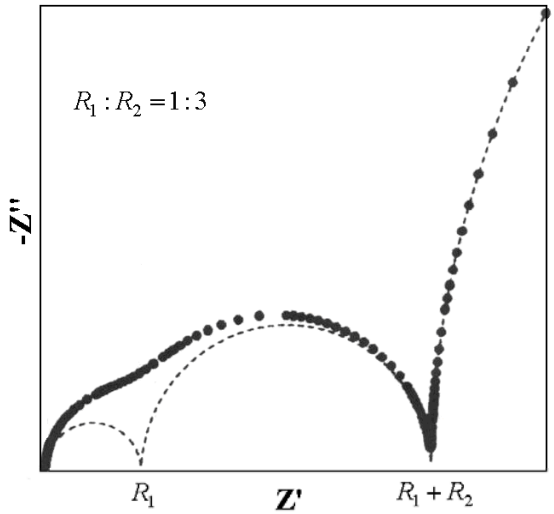

Figure 3. Cole-Cole plots for the model.

conduction mechanisms. One is the bulk conduction in the region of high frequencies. The other is the grain boundary diffusion in the region of low frequencies.

2.3. Ionic conductivity in LLTO

Figure 4 shows typical impedance plots of perovskite-type lithium ionic conductor LLTO at room temperature, in which the first semicircle is a bulk part. Because, we can understand the resistivity of bulk part is not dependent on the sample depth, although the second semicircle due to the grain boundary diffusion is dependent on the sample depth. In Fig. 5 we give an example of the bulk conductivity data extracted from the impedance plots in Fig.4. Some results from literatures have been added in Fig. 5 [4]. The ionic conductivity increases with increasing y concentration and temperature. The maximum ionic conductivity value was obtained around y = 0.21 and the conductivity kept high values at higher concentration. It may be of interest at this point to consider the ionic conduction mechanism.

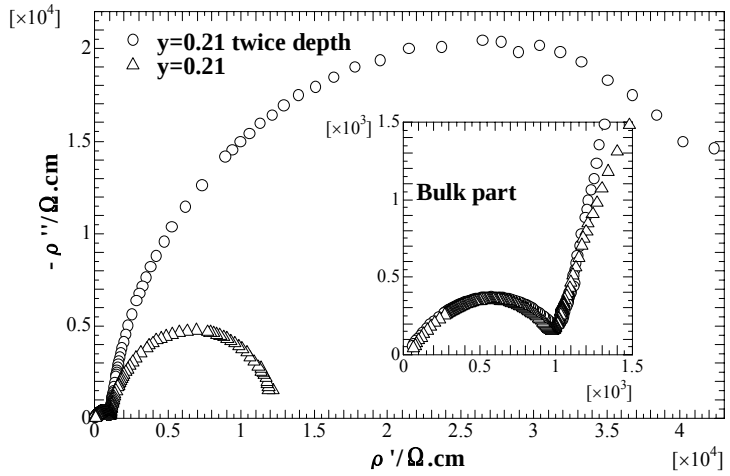

Figure 4. Cole-Cole plots of lithium ionic conductor LLTO. S' and S" are real and imaginary parts of resistivity, respectively.

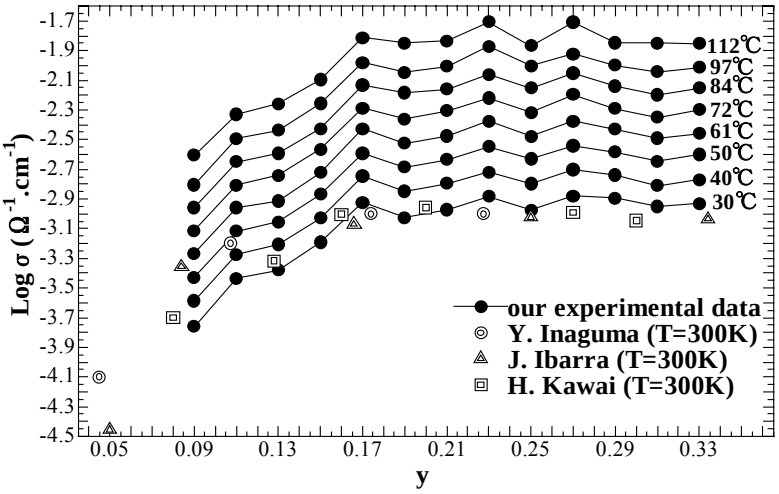

Figure 5. Ionic conductivity against y concentration.

3. X-ray diffraction and Rietveld analysis

3.1. Bragg reflection

It is well known that when X-rays pass through the crystal, the constructive reflection can be observed for a particular condition. The condition for the *n*-th reflection becomes

$$2d\sin\theta = n\lambda \quad \text{with} \quad n = 0,1,2,3,\cdots\cdots \tag{12}$$

where d is the distance between successive planes, θ the Bragg angle, λ the incident X-ray wavelength and n the order of reflection. The structure factor $F(hkl)$ for Miller indices (hkl) may be written

$$F(hkl) = \sum_i f_i e^{i2\pi(hu_i + kv_i + lw_i)} \tag{13}$$

where f_i is the atomic scattering factor of the i-th atom. The coordinates of the i-th atom can be represented by the vector $\boldsymbol{r}_i$ from the origin

$$\boldsymbol{r}_i = u_i \boldsymbol{a} + v_i \boldsymbol{b} + w_i \boldsymbol{c} \tag{14}$$

where $\boldsymbol{a}$, $\boldsymbol{b}$ and $\boldsymbol{c}$ are primitive cell parameters, and u_i, v_i and w_i are integers. The intensity of an X-ray diffraction I is proportional to the square of the structure factor $|F|^2 = FF^*$ where F* represents the complex conjugate of F. We may write

$$I = I_0 |F|^2 \tag{15}$$

where I_0 is the incident X-ray intensity.

3.2. Rietveld analysis

The Rietveld analysis is a technique of the least-squared refinements for obtaining the structure parameters [9,10]. The calculated intensities $f_c(x)$ are determined from the factor $|F_K|^2$ of structural model plus the background intensity y_b as the following

$$f_i(x) = sS_R(\theta_i)A(\theta_i)D(\theta_i)\sum_K m_K |F_K|^2 P_K L(\theta_K)\phi(2\theta_i - 2\theta_K) + y_b \tag{16}$$

where s is the scale factor, $S_R(\theta_i)$ the surface roughness factor, $A(\theta_i)$ the absorption factor, $D(\theta_i)$ the slit width factor, K the reflection number of Bragg peak, m_K the multiplicity factor, P_K the preferred orientation factor, $L(\theta_K)$ the Lorenz polarization factor, $\phi(2\theta_i\text{-}2\theta_K)$ the reflection profile function, $2\theta_i$ the diffraction angle and θ_K the Bragg angle. The quantity minimized in the least-squared refinement is the residual $S(x)$

$$S(x) = \sum_i w_i [y_i - f_i(x)]^2 \tag{17}$$

where $w_i (= 1/y_i)$ is the statistical weight, y_i the observed intensity at the i-th step ($2\theta_i$).

3.3. X-ray diffraction spectra in LLTO

Figure 6 shows an X-ray diffraction pattern observed for powdered LLTO (y = 0.21) and the calculated Rietveld's refinement profile at room temperature [4]. The refinement was carried out in tetragonal structure with space group $p4/mmm$. They are in good agreement. The bottleneck size is defined by the smallest cross-sectional area of the interstitial pathway that is constructed by four O^{2-} as shown in Fig. 7. Here, 1b-1b, 1a-1a and 1a-1b in tetragonal structure define the bottleneck sizes via the pathway from 1b to 1b, 1a to 1a and 1a to 1b, respectively. Figure 8 shows the bottleneck sizes against y concentration. As can be seen, the sizes of 1b-1b and 1c-1c bottleneck are larger than 1a-1a bottleneck size in low concentration [4]. Here, 1c-1c defines the bottleneck size in the orthorhombic structure for y = 0.09 – 0.15. The size

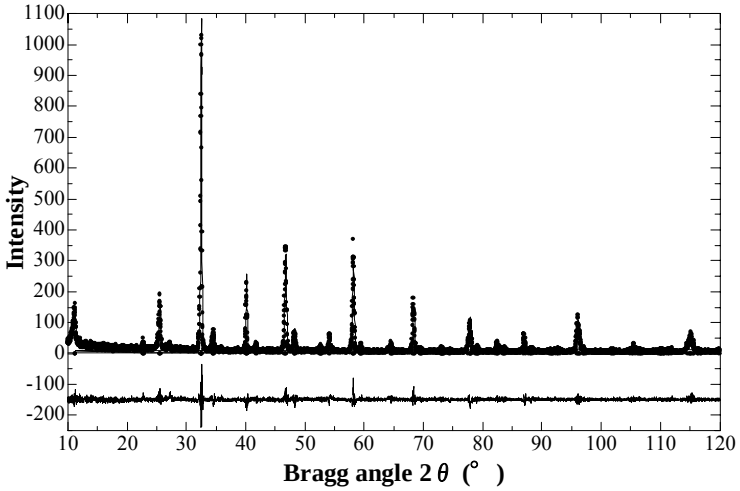

Figure 6. X-ray diffraction pattern and Rietveld's refinement profile.

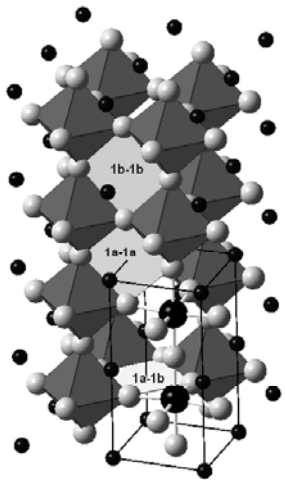

Figure 7. Crystal structure and bottleneck size of LLTO.

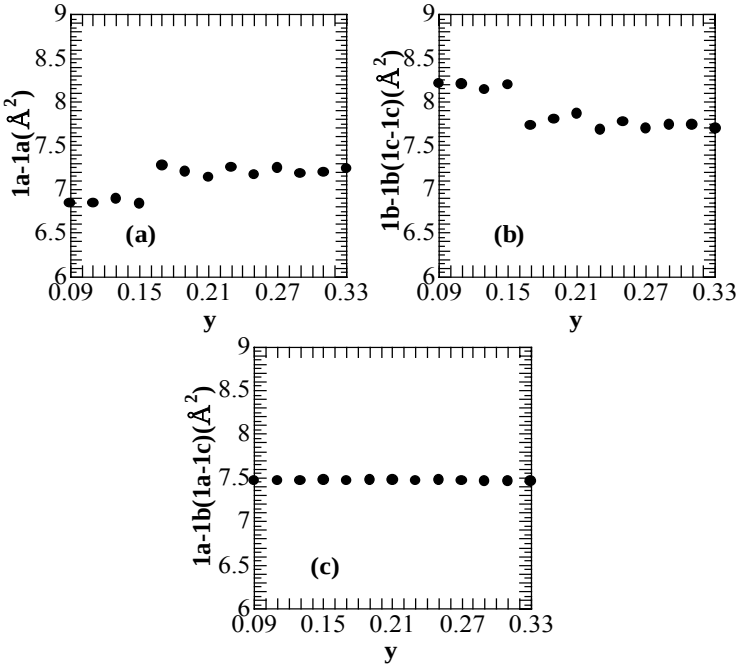

Figure 8. Bottleneck sizes against y concentration.

of 1b-1b bottleneck decreases with increasing *y* concentration and is comparable with 1a-1a and 1a-1b bottleneck sizes in high concentration. From aspects of bottleneck size and occupancy, lithium ion can easily migrate in 1b-1b and 1c-1c at low concentration. Further Discussion in high concentration will be done with the same way.

4. NMR

4.1. Nuclear magnetic moment

A magnetic moment $\boldsymbol{\mu}$ associated with an angular momentum $\hbar\boldsymbol{I}$ is given by

$$\mu = \gamma\hbar\boldsymbol{I} \tag{18}$$

where γ is the magnetogyric constant, $\hbar$ Planck's constant divided by 2π, and $\boldsymbol{I}$ the nuclear spin. When the magnetic moment $\boldsymbol{\mu}$ interacts with an external magnetic field $\boldsymbol{B}$, the Hamiltonian operator H is

$$H = -\boldsymbol{\mu} \bullet \boldsymbol{B}. \tag{19}$$

If the external magnetic field $\boldsymbol{B}_0$ is applied along the z direction, we have

$$H = -\gamma\hbar \boldsymbol{B}_0 \bullet \boldsymbol{I}. \tag{20}$$

The solutions of this Hamiltonian give energy levels

$$E = -\gamma\hbar \boldsymbol{B}_0 m \quad \text{with } m = I, I-1, \cdots\cdots, -I \tag{21}$$

where m is the magnetic quantum number.

4.2. Equation of motion

We consider an arbitrary direction for a single nuclear dipole μ relative to the magnetic field $\boldsymbol{B}_0$. The magnetic field produces a torque $\boldsymbol{\mu} \times \boldsymbol{B}_0$ on the dipole, so that, we have the gyroscopic equation

$$\hbar d\boldsymbol{I} / dt = \boldsymbol{\mu} \times \boldsymbol{B}_0 \tag{22}$$

Adding the effect of all dipole moment $\boldsymbol{M}$ in a unit volume, we rewrite the rate of change of $\boldsymbol{M}$

$$d\boldsymbol{M} / dt = \gamma \boldsymbol{M} \times \boldsymbol{B}_0. \tag{23}$$

When the component of dipole moment along the z direction M_z is not in the thermal equilibrium, the rate of change of M_z is assumed as

$$\frac{dM_z}{dt} = -\frac{M_z - M_0}{T_1} \tag{24}$$

where T_1 is the spin-lattice relaxation time, and M_0 the equilibrium value. Combining eq.(24) with the z-component of eq.(23), the equation of motion becomes

$$\frac{dM_z}{dt} = \gamma(\boldsymbol{M} \times \boldsymbol{B}_0)_z + \frac{M_0 - M_z}{T_1}. \tag{25}$$

Two other expressions for the rate of change of M_x and M_y are given by

$$dM_x / dt = \gamma(\boldsymbol{M} \times \boldsymbol{B}_0)_x - M_x / T_2 \tag{26}$$

$$dM_y / dt = \gamma(\boldsymbol{M} \times \boldsymbol{B}_0)_y - M_y / T_2 \tag{27}$$

where T_2 is determined by the spin-spin interaction, called by the transverse relaxation time. A set of equations (25)-(27) is the Bloch equations. Under the influence of a constant magnetic field $\boldsymbol{B_0}$ in the z direction and the oscillating magnetic field $\boldsymbol{B_1}$ in the x direction, solutions of the Bloch equations for M_z and M_x are given by

$$M_z = \chi_0 B_0 \frac{1+(\omega_0-\omega)^2 T_2^2}{1+(\omega_0-\omega)^2 T_2^2+\gamma^2 B_1^2 T_1 T_2} \tag{28}$$

$$M_x = \frac{1}{2}\chi_0 \omega_0 T_2 \frac{T_2(\omega_0-\omega)2B_1\cos\omega t + 2B_1 \sin\omega t}{1+T_2^2(\omega_0-\omega)^2+\gamma^2 B_1^2 T_1 T_2} \tag{29}$$

where χ_0 is the static susceptibility and $\omega_0 (= \gamma B_0)$ the angular resonance frequency.
If we defined the complex susceptibility χ^*, $M_x(t)$ becomes

$$M_x(t) = \chi'(2B_1\cos\omega t) + \chi''(2B_1 \sin\omega t) \tag{30}$$

where $\chi^* = \chi' - i\chi''$. The quantity χ' is called the dispersion. The quantity χ" determines the absorption of energy by the materials. Using eqs.(29) and (30), χ' and χ" are

$$\chi' = \frac{1}{2}\chi_0 \omega_0 T_2 \frac{(\omega_0-\omega)T_2}{1+(\omega_0-\omega)^2 T_2^2+\gamma B_1^2 T_1 T_2} \tag{31}$$

$$\chi'' = \frac{1}{2}\chi_0 \omega_0 T_2 \frac{1}{1+(\omega_0-\omega)^2 T_2^2+\gamma^2 B_1^2 T_1 T_2}\,. \tag{32}$$

Assuming the amplitude of the oscillating magnetic field is so small and $\gamma^2 B_1^2 T_1 T_2 \ll 1$, the half-width of the resonance at half maximum of the absorption is

$$(\Delta\omega)_{1/2} = 1/T_2\,. \tag{33}$$

4.3. Relaxation time and atomic motion

The spin-lattice relaxation time T_1 is represented by

$$\frac{1}{T_1} = C\frac{\tau}{1+\omega_0^2\tau^2} \tag{34}$$

where C is a constant and τ the correlation time. This is the well-known Bloembergen-Purcell-Pound (BBP) theory of the relaxation rate. The correlation time τ is defined by the thermally activated mean residence time of jumping ion

$$\tau = \tau_0 \exp(E_a / k_B T) \tag{35}$$

where E_a is the activation energy, k_B the Boltzmann constant, T the absolute temperature, $1/\tau_0$ the attempt frequency. The plot of log T_1 against $1/T$ for a constant frequency shows a V-shaped profile and gives us τ at temperature where T_1 shows a minimum. However, it is known that the BPP model is inadequate in many ionic conductors due to the reasons of (i) the log T_1 versus $1/T$ is not symmetrical, (ii) the activation energy does not agree with that obtained from the conductivity measurement, etc [12].

4.4. Line width

The line width of a resonance absorption spectrum is influenced by the magnetic dipole at rigid lattice. The effective magnetic field at the nucleus can be calculated from the classical magnetic dipole interaction formula. The effective magnetic field $\Delta\boldsymbol{B}$ produced by a magnetic dipole $\boldsymbol{\mu}_2$ at a point $\boldsymbol{r}$

$$\Delta\boldsymbol{B} = 3r^{-5}(\boldsymbol{\mu}_2 \bullet \boldsymbol{r})\boldsymbol{r} - \boldsymbol{\mu}_2 r^{-3}. \tag{36}$$

The order of the effective magnetic field at $\boldsymbol{r}$ from a rigid lattice of $\boldsymbol{\mu}$ is given by

$$\Delta B_{eff} \approx \mu r^{-3}. \tag{37}$$

4.5. Motional narrowing

The line width of resonance spectrum at high temperature decreases with increasing temperature. We may introduce an average time τ that a mobile ion remains in one site. When the temperature increases, τ decreases because of the high mobility. The transverse relaxation time T_2 is a dephasing time due to a local perturbation after initially a common phase. The line width for fast ion migration with an average time τ is given by

$$\Delta\omega = 1/T_2 = (\Delta\omega)_0^2\tau \tag{38}$$

where $(\Delta\omega)_0 = \gamma\Delta B$ is the line width due to the dipole interaction at the rigid lattice.

Figure 9 shows the ^{7}Li Static NMR spectrum in LLTO for $y = 0.33$. Using Lorentzian fitting the main central peak in $y = 0.33$ is easily divided into two parts: a narrow large intense peak and a small broad central peak [4]. The spectrum with a narrow intense is for a mobile lithium ion, and the ion plays the role of carrier in this structure. The lithium ion for the broad component can not migrate into lattice sites, and is called by an immobile ion.

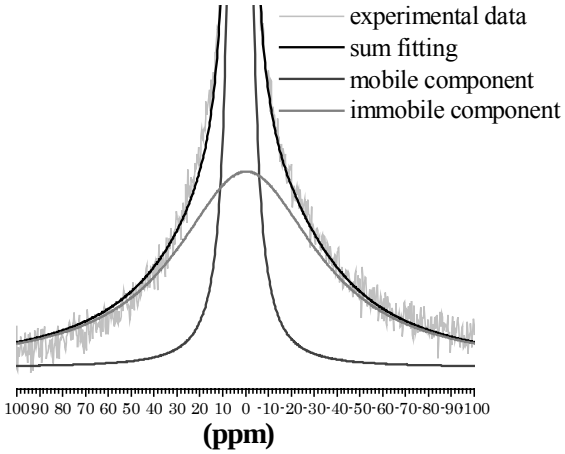

Figure 9. ^{7}Li Static NMR spectra in LLTO.

4.6. Chemical shifts

The chemical shift is due to the magnetic screening produced by electrons. The experiments of chemical shift have become a powerful tool in studying the molecular electronic structure and the structure of ionic conductors. The effective magnetic field at the nucleus is

$$\boldsymbol{B}_{\text{eff}} = \boldsymbol{B}_0(1-\sigma) \tag{39}$$

where $\boldsymbol{B}_0$ is the external field, σ the shielding factor. The resonance frequency ν_0 including the shielding factor σ becomes

$$\nu_0 = \frac{\gamma}{2\pi}\boldsymbol{B}_0(1-\sigma) \tag{40}$$

where γ is the magnetogyric ratio. The symbol δ is defined by

$$\delta = \frac{\nu_s - \nu_{\text{ref}}}{\nu_{\text{ref}}} \times 10^6 \tag{41}$$

where v_s and v_{ref} are the resonance frequencies of sample and reference, respectively. Using eqs. (39) and (40) δ becomes

$$\begin{aligned}\delta &= \frac{(1-\sigma_s)-(1-\sigma_{ref})}{(1-\sigma_{ref})}\times 10^6 \\ &\approx (\sigma_{ref}-\sigma_s)\times 10^6\end{aligned} \tag{42}$$

where σ_s and σ_{ref} are the shielding factors of sample and reference, respectively. If a nucleus has a larger shielding factor, a higher applied field is needed.

In a spherical symmetry of *S* electronic state, the magnetic shielding factor was calculated by Lamb. His theory was applicable only to a single free atom of *S* state. Ramsey accounted for the shielding factor due to electronic motion in a molecule. The shielding factor was expressed by a sum of the diamagnetic part σ_d and the paramagnetic part σ_p

$$\sigma = \sigma_d + \sigma_p . \tag{43}$$

The first term σ_d is the same factor obtained by Lamb. The second term σ_p is due to the presence of *p* or *d* electrons near the nucleus. The local diamagnetic term σ_d of a hydrogen atom in a molecule can be estimated from Lamb formula

$$\sigma_d(local) = 17.8\times 10^{-6}\lambda \tag{44}$$

where λ measures the effective number of electrons in the 1*S* orbital of the hydrogen. From eq. (44) chemical shifts for hydrogen in various functional groups are in the range of a few ppm. This suggests that variations in the electron density around the proton give changes in the shielding factor.

The magnetic dipole moment of proton experiences a considerable magnetic field due to the local atom X bonded to the hydrogen H. This is the neighbor anisotropy effect. Pople estimated the magnitude of such an effect at the proton H due to point magnetic dipoles in the other atom [13]. The mean proton chemical shift is

$$\begin{aligned}\Delta\sigma &= \frac{1}{3}R^{-3}\sum_{i=1,2,3}\chi^{(i)}_{atomic}(1-3\cos^2\gamma_i) \\ &= \frac{1}{3R^3H_0}\sum_{i=x,y,z}\mu_i(1-3\cos^2\gamma_i)\end{aligned} \tag{45}$$

where $\chi^{(i)}_{atomic}$ is the *i*-th principal susceptibility of X atom in the directions which make angle γ_i with the XH line, *R* the XH distance, H_0 the applied

magnetic field and $\mu_i (= \chi^{(i)}_{atomic} \bullet H_0)$ the magnetic dipole. If H_0 is along the i direction, the induced magnetic dipole moment is $\chi^{(i)}_{atomic} H_0$. Pople showed the formula that the μ_x, μ_y and μ_z were given by the energy difference $\overline{\Delta E}$ between excited and ground states of X atom, and the Mulliken's population associated with $2p_x$, $2p_y$ and $2p_z$ atomic orbitals of X atom, etc. This theory was in good agreement with the experimental chemical shift in water.

The electron configuration of lithium consists of 2*S* orbital. The chemical shifts due to Lamb and Ramsey theories seem to be small as the same with those in proton. Figure 10 shows ^{7}Li MAS NMR spectra of LLTO dependent on *y* concentration [15]. This seems to be the neighbor anisotropy effect. The value of chemical shift may be possible to be calculated on the base of Pople theory.

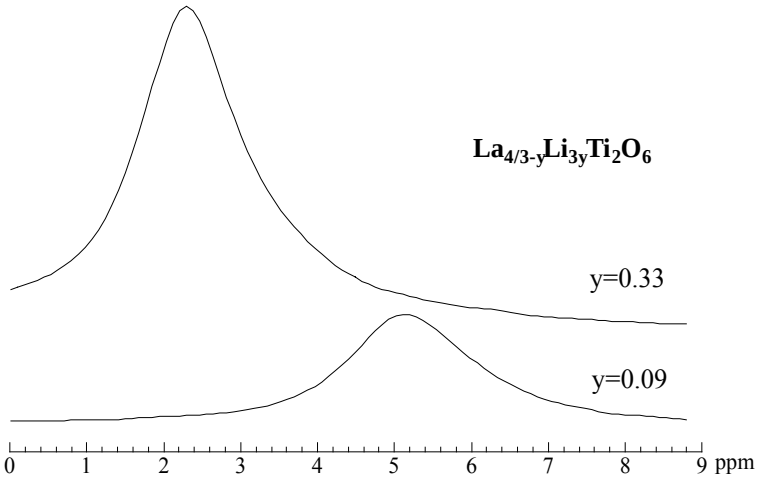

Figure 10. ^{7}Li MAS NMR spectra of LLTO dependent on *y* concentration.

4.7. Quadrupole interaction

The nuclear electric quadrupole moment for nuclei with $I \geqq 1$ interacts with an electrostatic field gradient produced by electric charges around the nucleus [14]. The quadrupole Hamiltonian H_Q can be expressed

$$H_Q = \frac{1}{6} \sum_{j,k} Q_{jk} V_{jk} \tag{46}$$

where Q_{jk} is the quadrupole tensor, V_{jk} the electric field gradient and j, $k = x$, y, z. When the nuclear spin is quantized along the z direction, eQ is defined by

$$eQ = \int (3z^2 - r^2) \rho(\boldsymbol{r}) dv \tag{47}$$

where eQ is the electric quadrupole moment measured in units of the charge e and $\rho(\boldsymbol{r})$ the nuclear charge density. In terms of the quantum mechanical argument, the quadrupole Hamiltonian H_Q becomes

$$H_Q = \frac{eQ}{6I(2I-1)} \sum_{j.k} V_{jk} \{\tfrac{3}{2}(I_j I_k + I_k I_j) - \delta_{jk} \boldsymbol{I}^2\}. \tag{48}$$

In terms of I_z *and* $I_\pm (= I_x \pm i I_y)$ the matrix element of the quadrupole Hamiltonian gives

$$\left\langle m' \middle| H_Q \middle| m \right\rangle = \frac{eQ}{4I(2I-1)} \left\langle m' \middle| (3I_z^2 - \boldsymbol{I}^2)V_0 + (I_+ I_z + I_z I_+)V_{-1} + (I_- I_z + I_z I_-)V_1 + I_+^2 V_{-2} + I_-^2 V_2 \middle| m \right\rangle \tag{49}$$

where $V_0 = V_{zz}$, $V_{\pm 1} = V_{xz} \pm i V_{yz}$, $V_{\pm 2} = \frac{1}{2}(V_{xx} - V_{yy}) \pm i V_{xy}$. (50)

All the matrix elements of the quadrupole Hamiltonian are

$$\begin{aligned}
&\left\langle m \middle| H_Q \middle| m \right\rangle = \mathrm{A}\{3m^2 - I(I+1)\}V_0 \\
&\left\langle m \pm 1 \middle| H_Q \middle| m \right\rangle = \mathrm{A}(2m \pm 1)\{(I \mp m)(I \pm m + 1)\}^{\frac{1}{2}} V_{\mp 1} \\
&\left\langle m \pm 2 \middle| H_Q \middle| m \right\rangle = \mathrm{A}\{(I \mp m)(I \mp m - 1)(I \pm m + 1)(I \pm m + 2)\}^{\frac{1}{2}} V_{\mp 2}
\end{aligned} \tag{51}$$

where $\mathrm{A} = \dfrac{eQ}{4I(2I-1)}$.

By choosing orthogonal principal axes x', y', z' the relation satisfies at the nuclear site

$$\nabla^2 V = V_{x'x'} + V_{y'y'} + V_{z'z'} = 0. \tag{52}$$

Thus there are two independent parameters. We can take the principal axes as the maximum of $V_{z'z'}$ and the x' axis along the direction of minimum electric field gradient as the followings

$$\left|V_{z'z'}\right| \geq \left|V_{y'y'}\right| \geq \left|V_{x'x'}\right|. \tag{53}$$

Two parameters q and η are defined by

$$eq \equiv V_{z'z'} = \left(\frac{\partial^2 V}{\partial z'^2}\right)_0 \tag{54}$$

$$\eta \equiv (V_{x'x'} - V_{y'y'}) / V_{z'z'} \qquad (55)$$
$$0 \le \eta \le 1.$$

The parameter η is called the asymmetry parameter. If the field gradient has a cubic symmetry, the quadrupole interaction vanishes.

We can treat the total Hamiltonian H

$$H = H_M + H_Q \qquad (56)$$

where H_M gives the magnetic energy levels shown in eq. (21), H_Q the quadrupole interaction as the perturbation. The energy levels are

$$E_m = \sum_{k \ge 0} E_m^{(k)} \qquad (57)$$

where $E_m^{(k)}$ is the magnetic energy levels due to the k-th order perturbation. The strength of the quadrupole interaction (= frequency) is defined by

$$\nu_Q = 3e^2 qQ / 2I(2I-1)h. \qquad (58)$$

The perturbation calculation yields the formulas for the first-order perturbation

$$E_m^{(1)} = \left\langle m \middle| H_Q \middle| m \right\rangle = h\nu_Q \tfrac{1}{2} f_0 (m^2 - \tfrac{a}{3}) \qquad (59)$$

for the second-order perturbation

$$E_m^{(2)} = \frac{\left|\left\langle m \middle| H_Q \middle| m-1 \right\rangle\right|^2}{E_m^0 - E_{m-1}^0} + \frac{\left|\left\langle m \middle| H_Q \middle| m+1 \right\rangle\right|^2}{E_m^0 - E_{m+1}^0} + \frac{\left|\left\langle m \middle| H_Q \middle| m-2 \right\rangle\right|^2}{E_m^0 - E_{m-2}^0} + \frac{\left|\left\langle m \middle| H_Q \middle| m+2 \right\rangle\right|^2}{E_m^0 - E_{m+2}^0}$$

$$= -\frac{\nu_Q^2 h}{12\nu_0} m\{|f_1|^2 (8m^2 - 4a + 1) + |f_2|^2 (-2m + 2a - 1)\} \qquad (60)$$

where $a = I(I+1)$, $V_0 = eqf_0, V_{\pm 1} = eqf_{\pm 1}$ *and* $V_{\pm 2} = eqf_{\pm 2}$.

Here, we choose the principal axes, x', y', z' relative to the symmetry axes x, y, z, and treat with the symmetric field gradient ($\eta = 0$). The transformations of f from the principal axes to the x, y, z axes were given by Cohen et al [14].

$$f_0 = \frac{1}{2}(3\cos^2\theta - 1)$$
$$f_{\pm 1} = \sqrt{3/2}\sin\theta\cos\theta\exp(\pm i\phi) \quad (61)$$
$$f_{\pm 2} = \frac{1}{2}\sqrt{3/2}\sin^2\theta\exp(\pm 2\phi).$$

We consider the magnetic resonance corresponding to transitions with $|\Delta m| = 1$. The resonance frequencies $\nu_m = (E_{m-1} - E_m)/h$ for the first-order perturbation is

$$\nu_m^{(1)} = -(m - \tfrac{1}{2})\nu_Q(\tfrac{3}{2}\mu^2 - \tfrac{1}{2}) \quad (62)$$

where $\mu = \cos\theta$.

The frequency of the central component for the second-order perturbation is

$$\nu_{1/2}^{(2)} = -(\nu_Q^2/16\nu_0)(a - \tfrac{3}{4})(1 - \mu^2)(9\mu^2 - 1). \quad (63)$$

The random distribution of orientations in a powdered sample gives rise to a continuous distribution of resonance frequencies. The normalized shape function $g_m(\nu)$ for the m-th frequency in the first-order perturbation is given by

$$g_m(\nu) = 2P(\mu)\left|\frac{d\mu}{d\nu}\right| \quad (64)$$

where $P(\mu)$ is the probability between μ and $\mu + d\mu$. Here, we consider $I = \frac{3}{2}$. Using eq. (62), the frequency for the first-order perturbation $(m \neq \frac{1}{2})$ is

$$\nu = \nu_0 - \frac{1}{2}\nu_Q(m - \tfrac{1}{2})(3\cos^2\theta - 1). \quad (65)$$

Then, μ is given by

$$\mu = \cos\theta = \frac{1}{\sqrt{3}}\{1 - \frac{\nu - \nu_0}{\frac{1}{2}\nu_Q(m - \frac{1}{2})}\}^{\frac{1}{2}} \quad (66)$$

so that

$$g_m(\nu) = \left|\frac{d\mu}{d\nu}\right| = \left|\frac{1}{\sqrt{3}\nu_Q(m - \frac{1}{2})}\right|\{1 - \frac{\nu - \nu_0}{\frac{1}{2}\nu_Q(m - \frac{1}{2})}\}^{-\frac{1}{2}}. \quad (67)$$

The solutions are three cases;

(a) $m = 3/2$ $\left(m = \frac{3}{2} \rightarrow \frac{1}{2}\right)$

$$g_{\frac{3}{2}}(\nu) = \sqrt{\frac{1}{\nu_Q}}\{(\nu_0 + \tfrac{\nu_Q}{2}) - \nu\}^{-\frac{1}{2}} \quad \text{for } \nu_0 - \nu_Q \le \nu < \nu_0 + \tfrac{\nu_Q}{2} \tag{68}$$

(b) $m = -1/2$ $\left(m = -\frac{1}{2} \rightarrow -\frac{3}{2}\right)$

$$g_{-\frac{1}{2}} = \sqrt{\frac{1}{6\nu_Q}}\{\nu - (\nu_0 - \tfrac{1}{2}\nu_Q)\}^{-\frac{1}{2}} \qquad \text{for } \nu_0 - \tfrac{1}{2}\nu_Q < \nu \le \nu_0 + \nu_Q \tag{69}$$

(c) $m = 1/2$ $\left(m = \frac{1}{2} \rightarrow -\frac{1}{2}\right)$

$$g_{\frac{1}{2}}(\nu) = \delta(\nu - \nu_0). \tag{70}$$

Using eq.(63), the frequency for the second-order perturbation is

$$\nu - \nu_0 = -\frac{1}{16}\frac{\nu_Q^2}{\nu_0}(a - \tfrac{3}{4})(1 - \mu^2)(9\mu^2 - 1). \tag{71}$$

Setting $y = \{(a - \frac{3}{4})\nu_Q^2 / 16\nu_0\}^{-1}(\nu - \nu_0),$ we obtain

$$y = 9\mu^4 - 10\mu^2 + 1. \tag{72}$$

The solutions of eq. (72) are

$$\mu^2 = \frac{5 \pm 3z}{9} \tag{73}$$

where $z = \sqrt{\frac{16}{9} + y}.$ (74)

The equations of (73) are

$$\mu^2 = \frac{5 + 3\sqrt{\frac{16}{9} + y}}{9} \qquad \text{for} \quad -\tfrac{16}{9} \le y \le 0 \tag{75}$$

$$\mu^2 = \frac{5 - 3\sqrt{\frac{16}{9} + y}}{9} \qquad \text{for} \qquad 0 \le y \le 1. \tag{76}$$

By using $g(\nu) = \frac{d\mu}{d\nu} = \frac{d\mu}{dz}\frac{dz}{dy}\frac{dy}{d\nu}$, the second order patterns *g(ν)* are given by three cases;

(a) case 1

$$g(\nu) = \frac{1}{A}\{(5+3z)^{-\frac{1}{2}} + (5-3z)^{-\frac{1}{2}}\}\frac{1}{4z} \quad \text{for } \nu_0 - \tfrac{16}{9}A \le \nu \le \nu_0 \tag{77}$$

where $A = \frac{\nu_Q^2}{16\nu_0}(a - \frac{3}{4})$

(b) case 2

$$g(\nu) = \frac{(5-3z)^{-\frac{1}{2}}}{4z}A^{-1} \quad \text{for } \nu_0 \le \nu \le \nu_0 + A \tag{78}$$

(c) case 3

$$g(\nu) = 0 \quad \text{elsewhere.} \tag{79}$$

Figures 11 and 12 show the first and second-order powder patterns for symmetrical gradient ($\eta = 0$) obtained by eqs. (62) - (79), respectively.

The computer simulated methods for the first- and second-order powder patterns with arbitrary qQ and η are given by Massiot et al [16]. They are

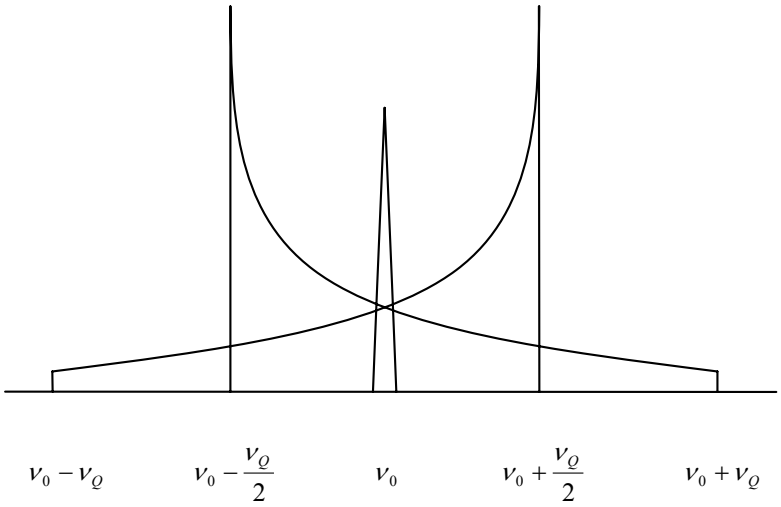

Figure 11. First-order powder patterns for $\eta = 0$.

useful for fitting NMR spectra due to the quadrupole effect. We calculated powder patterns for I=3/2 by the first-order perturbation depending on η and $e^2qQ/2h$ in MAS NMR. Figure 13 shows the first-order powder patterns. Figure 14 shows the second-order powder patterns depending on η and

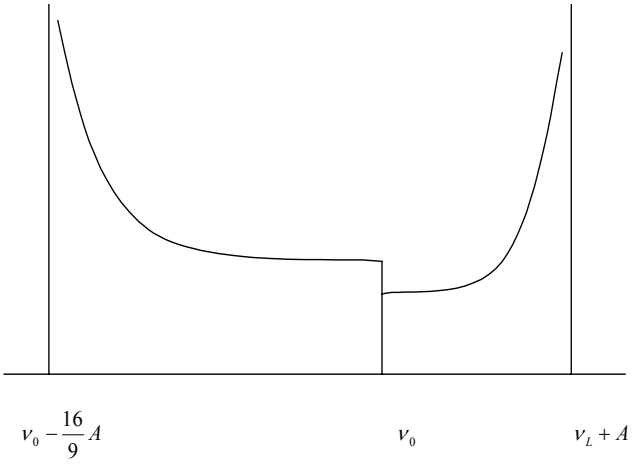

Figure 12. Second-order powder patterns for η = 0

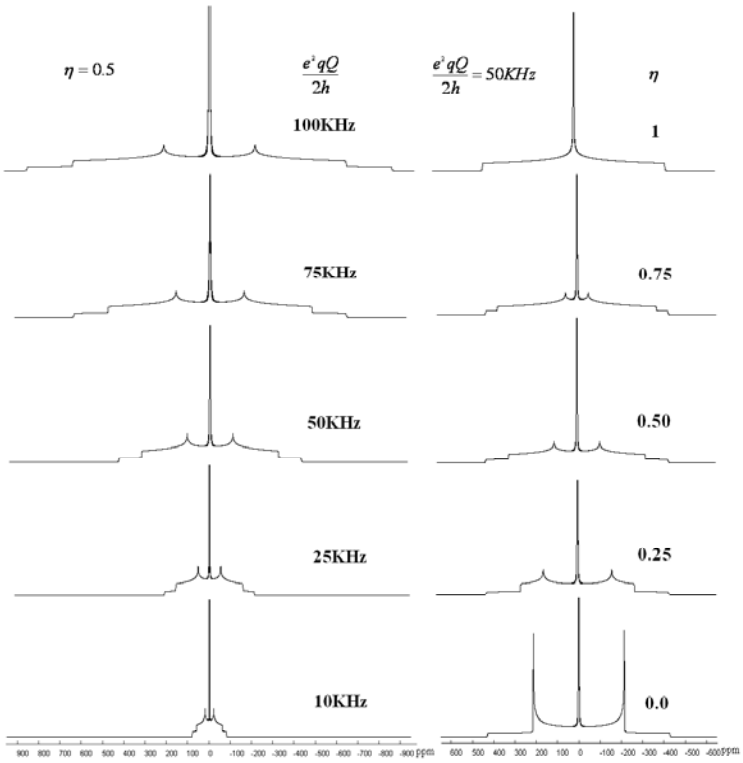

Figure 13. First-order simulated powder patterns depending on η and $e2qQ/2h$ for I = 3/2 in MAS NMR.

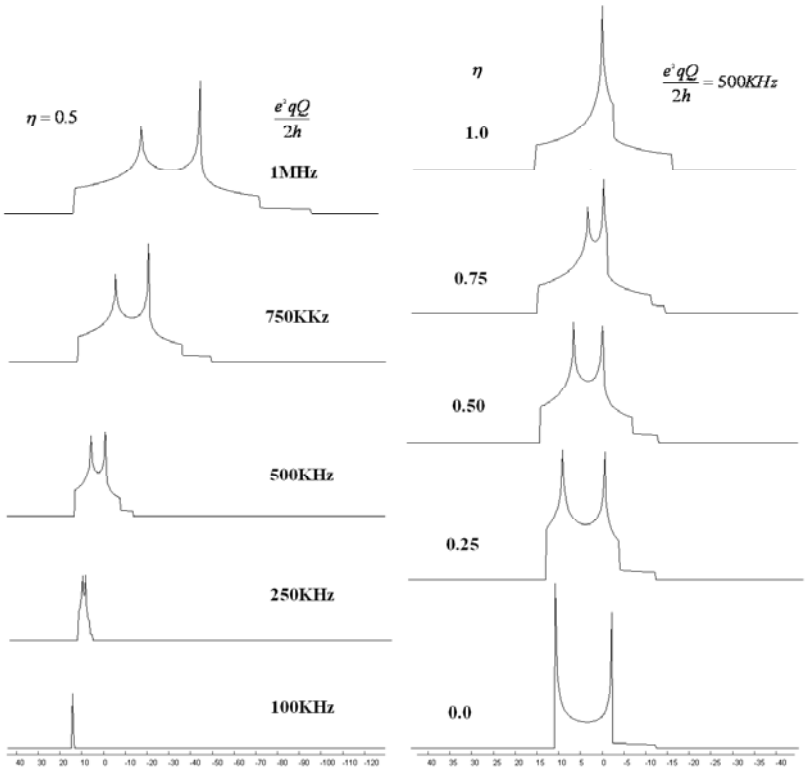

Figure 14. Second-order simulated powder patterns depending on η and $e2qQ/2h$ for I = 3/2 in MAS NMR.

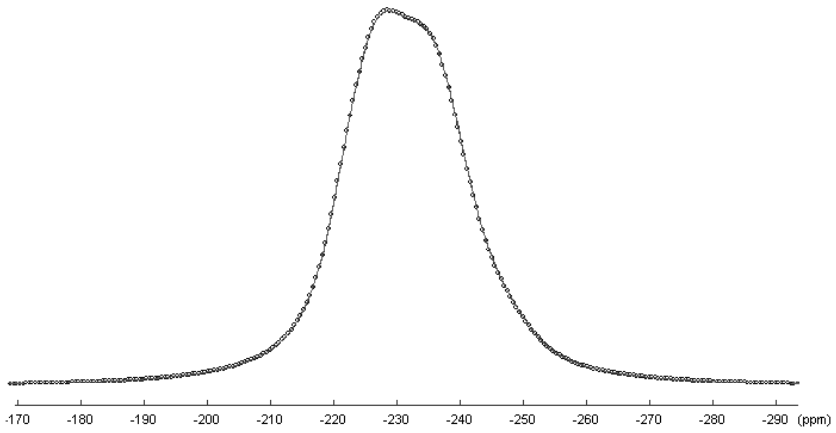

Figure 15. ^{27}Al MAS NMR spectrum in Al-*B* site substituted LLTO.

$e^2qQ/2$h in MAS NMR. Figure 15 shows a typical example of MAS NMR for ^{27}Al (I = 5/2) in Al-*B* site substituted LLTO with numerical values η = 0.35 and ν_Q = 539.8 kHz. The experimental solid line is in an excellent agreement with the dotted line calculated by Massiot fitting program [17].

5. Summary

Perovskite-type oxides are important from aspects of the fundamental research and applications to lithium ionic conductor, proton conductor, etc. We described the crystal structure of perovskite –type oxides, the ionic conduction with defects, the electric impedance measurements, the principles of X-ray diffraction and Rietveld analysis, the basis of NMR spectra. We showed properties of lithium ionic conductor of LLTO obtained by impedance measurement, X-ray diffraction, Rietveld analysis and NMR spectra.

References

1. Belous A.G., Novitskaya G.N., Polyanetskaya S.V., and Gornikov Yu.I., 1987, Izv. Akad. Nauk SSSR. Neorg. Mater., **23**, 470.
2. Inaguma Y., Chen L., Itoh M., Nakamura T., Uchida T., Ikuta H., and Wakihara M., 1993, Solid State Commun., **86**, 689.
3. Stramare S., Thangadurai V., and Weppner W., 2003, Chem. Mater., **15**, 3974.
4. Zou Y., and Inoue N., 2003, The 1st International Discussion Meeting on Superionic Conductor Physics, Abstracts, p.53, to be published in Proceedings 2005.
5. Iwahara H., 1992, Solid State Ionics, **52**, 99.
6. Kudo T., and Fueki K., 1990, Solid State Ionics, T. Kudo and K. Fueki (Ed.), Kodansya, Tokyo, p.113, p.133, p.192.
7. Ukshe E., Ukshe A., and Bukun N., 1991, Materials Science Forum, **76**, 213.
8. Kittel C., 1996, Introduction to Solid State Physics, 7th ed., Wiley, New York, Chap. 2.
9. Rietveld H.M., 1969, J. Appl. Crystallogr., **2**, 65.
10. Izumi F., 2002, Funmatsu X Senn Kaiseki no Zissai-Rietveld Nyumon (in Japanes), I. Nakai and F. Izumi (Ed.), Asakura Shoten, Tokyo.
11. Becker E.D., 2000, High Resolution NMR, Theory and Chemical Applications, Third Edition, Academic Press, London.
12. Brinkmann D., 1992, Progress in NMR Spectroscopy, **24**, 527.
13. Pople J.A., Schneider W.G., and Bernstein H.J., 1959, High Resolution Nuclear Magnetic Resonance, McGrow-Hill Book Co., Inc., New York, p.165.
14. Cohen M.H., and Reif F., 1957, Quadrupole Effects in Nuclear Magnetic Resonance Studies of Solids, **5**, 321.
15. Zou Y., Inoue N., 2004, Cyuugoku and Sikoku Sibu Meeting Abstracts of the Physical Society of Japan, Ea1-4, page 75, (in Japanese).
16. Massiot D., Fayon F., Capron M., King I., Calvé S.L., Alonso B., Durand J.-O., Bujoli B., Gan Z., and Hoatson G., 2002, Magn. Resn. Chem., **40**, 70.
17. Zou Y., and Inoue N., 2005, Meeting Abstracts of Physical Society of Japan, **60**, 25pYH-7, page 706 (in Japanese) Zou Y., and Inoue N., 2005, Solid State Ionics, 176, 2257.